Cu_2O Nano-flowers/Graphene Enabled Scaffolding Structure Catalyst Layer for Enhanced CO_2 Electrochemical Reduction

Yucheng Wang[1], Hanhui Lei[1], Shun Lu, Ziming Yang, Ben Bin Xu, Lei Xing, Terence Xiaoteng Liu**

Dr. Yucheng Wang, Hanhui Lei, Prof. Ben Bin Xu, Dr. Terence Xiaoteng Liu
Faculty of Engineering and Environment, Northumbria University, Newcastle upon Tyne, NE1 8ST, United Kingdom

Dr. Shun Lu
Department of Agricultural and Biosystems Engineering, South Dakota State University, Brookings, SD 57007, USA

Dr. Ziming Yang, Dr. Lei Xing,
Department of Engineering Science, University of Oxford, Oxford OX1 3PJ, United Kingdom

[1]authors contributed equally to this work.

To whom correspondence should be addressed:

Dr. Terence Xiaoteng Liu: terence.liu@northumbria.ac.uk

Dr. Lei Xing: xinglei1314@gmail.com

ABSTRACT:

Nanosized Cu_2O catalysts with precisely controlled bud-to-blooming flower shapes are synthesised using modified polyol method. The evolution of the shape when the catalysts are applied to the gas diffusion electrodes improves the key factors influencing the catalyst layer, e.g. volume porosity and triple-phase boundary contact areas. Numerical and experimental studies revealed increased reactant molar concentration and improved CO_2 mass transfer due to the structural changes, which influenced the electrochemical CO_2 reduction reaction (eCO_2RR). The fully bloomed Cu_2O nanoflower catalyst, combined with the two-dimensional (2D) structured graphene sheet, formed a catalyst layer with scaffolding structure that exhibited the highest Faradaic efficiency (FE) of 93.20% towards CO at an applied potential of −1.0 V vs. RHE in 1M KOH. These findings established the relationship between the catalyst layer properties and mass transfer, based on which we could describe the effect of the structural design of the catalyst layer on the eCO_2RR performance.

Keywords: *CO_2 reduction reaction, catalyst layer, nanoflower, graphene and modelling.*

1. INTRODUCTION

The 'net zero' target act has urged the development of carbon capture and utilisation technologies, including direct carbon capture [1, 2], enhanced weathering [3, 4], photochemical CO_2 conversion [5, 6] and electrochemical reduction [7, 8]. The electrochemical conversion of carbon dioxide (CO_2) has attracted increasing research attention owing to its many advantages, such as moderate reaction temperature, simple reaction setup, and high energy-density fuel products (e.g. CO and formate), and is one of the most efficient methods for large-scale energy storage, chemical production, and transportation systems [8, 9]. Moreover, electrochemical CO_2 reduction reaction (eCO_2RR) is a controllable process, and different products can be obtained by varying the catalyst architecture, electrolyte pH, applied potential, and electrolyser design etc. [10]. The commercialisation of this technology depends on a high-performance, stable catalyst. Significant effort has been made to overcome the challenges faced by catalysts, such as low catalytic activity [11, 12], low selectivity [13, 14], and poor durability of the reaction system [15, 16], which reduces the reaction efficiency. Inertness of CO_2 molecules requires high activation potential [17-19], and the low solubility (~35 mM at 298 K, 1 atm) of CO_2 in the electrolyte reduces the CO_2 mass transfer leading to hydrogen evolution reaction (HER) [20-22].

Significant research has been done over the last few decades to design novel electrocatalysts with enhanced Faradaic efficiency (FE) for a desired eCO_2RR product by controlling catalyst element selection [7], surface morphology [23], particle size [24], crystallisation [25] and architecture [26]. (1) The metallic catalysts for eCO_2RR with different elemental types afford different products through different reaction routes [15]. The binding energy difference of the *CO species in metallic electrocatalysts determines the selectivity of main products [27]. Although noble metals, such as Au, Ag, and Pt, exhibit better CO_2 selectivity toward CO than other metallic catalysts under moderate overpotentials [28], their high cost prohibits their commercialisation. Compared to noble metals, Cu has a low price and significant eCO_2RR activity [8], and is the only metal that yields multiple products, such as CO, formate, methane, ethane, ethylene, ethyne, methanol, ethanol and other C_2, or even C_3 organic products [29]. The selectivity of Cu-based catalysts depends on the catalyst morphology, local pH, overpotential, and electrolyte concentration [9]. Therefore, the reaction conditions should be carefully controlled to enhance the system selectivity. Cu oxide nanoparticles, such as cuprous oxide (Cu_2O), have attracted significant attention owing to their relatively high reaction activity for the conversion of CO_2 into CO, CH_4, or C_2 [30, 31] at relatively low applied potentials. (2) The morphology of the catalyst can be tuned to enhance the catalytic reaction efficiency, with specific morphological and electronic characteristics improving the selectivity and activity of eCO_2RR. Hu et al.[32] reported a unique shape of bismuth-based nanosheets on flow-through hollow fibre, with enhanced formate selectivity and activity, up to 85% with current density of

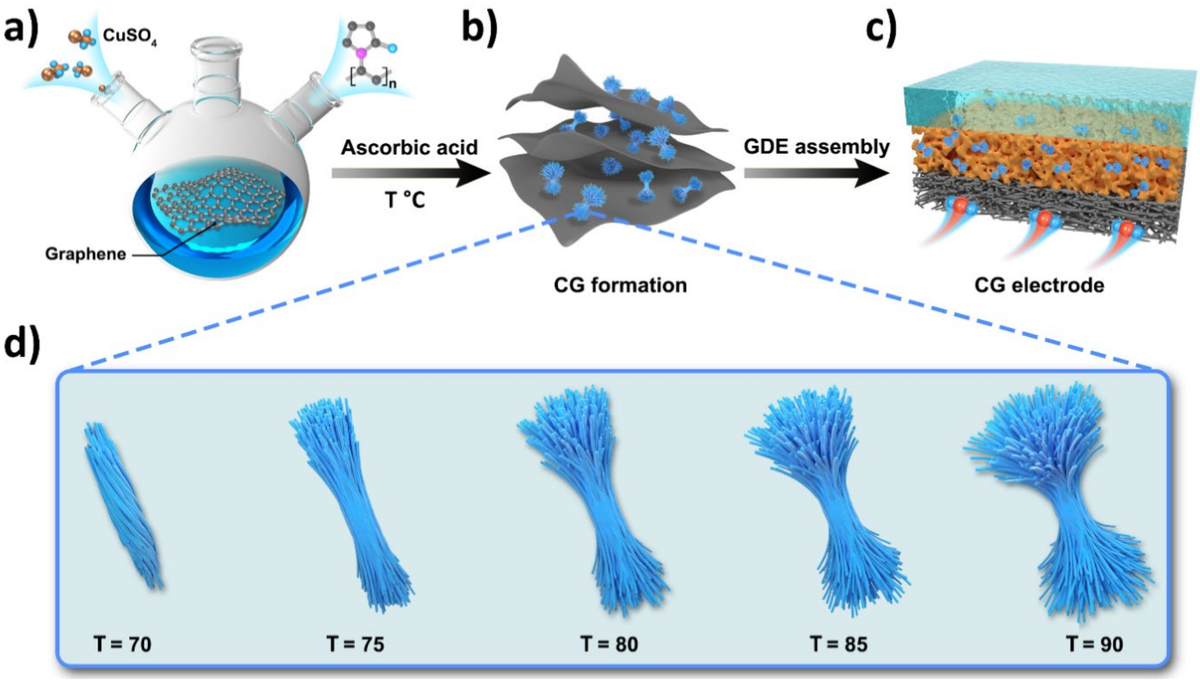

Figure 1 Scheme of CG electrodes for eCO_2RR. a) Modified polyol method for CG synthesis; b) CG formation on graphene layer; c) GDE assembly of CG electrode. d) Morphology of Cu_2O in CG by controlling the reaction temperature from 70 °C to 90 °C, where T (°C) represents the synthesis temperature.

141 mA cm^{-2} at −1.0 V vs. RHE. Jiao et al.[33] developed a Pd octahedra catalyst, represents up to 95% FE of CO and better reaction activity than Pd cubes.

The CO_2 mass transfer influences the efficiency of the reaction system. Recently, gas diffusion electrode (GDE) cells have been employed [22, 34] for eCO_2RR, where CO_2 is fed directly through the gas diffusion layer to the catalyst layer surface, with a short diffusion distance for the gaseous reactants to reach the electroactive sites on the catalyst surface [35]. Wang et al. [36] discovered a bilayer porous electrode with directional diffusion of gas molecules onto the catalyst layer and 94% FE to carbonaceous products at −1.0 V vs. RHE and a current density of 200 mA cm^{-2}. Dinh et al. [34] developed a polymer-based hydrophobic gas diffusion electrode, which prevents flooding and has a stable catalyst surface on account of the carbon nanoparticles and graphite, and exhibits 70% FE towards ethylene at −0.55 V vs. RHE. Although the effects of the electrode structure and catalyst layer have been reported, the effects of reduced mass transfer, porosity, and hydrophobicity of the catalyst-coated electrode on the performance have not yet been studied.

A high-performance catalyst with considerable CO_2 mass transfer is required for an effective reaction system. In this study, we synthesised a series of Cu_2O/graphene (CG) nanoflower composite catalysts with precise bud-to-blooming flower opening degrees. The degree of opening increases at each 5 °C along with temperature increase in synthesis temperature from 70 to 90 °C for each catalyst (**Figure 1**). The catalysts were printed on GDE as cathode catalyst layers and assembled in a 3D-printed cell to study the effect of the induced mass transfer. The fully bloomed nanoflower forms a scaffolding structure with the graphene sheets (Figure 1b), and one such structure was assembled as the CG electrode. This resulted in a change in the catalyst layer porosity (Figure 1c, orange middle layer), and the blooming flower petals increased the exposure of Cu_2O active sites compared to the buds resulting in an improved surface/volume ratio.

2. EXPERIMENTAL

2.1 Reagents

All the reagents were of analytical grade and were used without further purification. Copper (II) sulfate pentahydrate ($CuSO_4$•$5H_2O$, Sigma-Aldrich) was used as the copper precursor to prepare the catalyst. Graphene powder was purchased from Goodfellow. Ethylene glycol ($C_2H_6O_2$) was purchased from Fisher Scientific (U.K.). Polyvinylpyrrolidone (powder, wt. 10000) and L-ascorbic acid (powder) were purchased from Sigma Aldrich.

2.2 Catalyst Synthesis

The CG catalysts were synthesised using a modified polyol method. Initially, 53.5 mg of graphene, 150 mg of L-ascorbic acid (99%, in 20 mL deionised water) solution, and 80 mL ethylene glycol were mixed in a beaker and sonicated at 25 °C for 30 min to remove any oxide formed on graphene. The suspension was transferred into a three-neck flask, and 200 mL of ethylene glycol was added. Subsequently, polyvinylpyrrolidone (50 mg) was dissolved in 50 mL of deionised water and added to the flask. After that, 200 mg of $CuSO_4$•$5H_2O$ (Cu:C = 1:1 (wt.%)) was dissolved in 20 mL of deionised water and added to the flask dropwise. The mixture was then stirred at 400 rpm for 10 h in N_2 atmosphere at 70 °C, 75 °C, 80 °C, 85 °C, and 90 °C to obtain flower-like catalysts with different blooming degrees. The suspension was then filtered and washed with ethanol to remove the residual chemicals. A brief schematic of the synthesis procedure is illustrated in Figures 1 a, b, and d. Finally, the as-prepared catalysts were dried in an open-air oven at 40 °C. The catalysts were annotated as CG1, CG2, CG3, CG4, and CG5, corresponding to synthesis temperatures of 70, 75, 80, 85, and 90 °C, respectively. We also synthesised a Cu_2O nanocube catalyst without graphene (which provides a dense catalyst layer for eCO_2RR) to verify the effect of the catalyst layer structure using a previously reported synthesis method [36].

2.3 Physical Characterisation

Scanning electron microscopy (SEM), combined with energy-dispersive X-ray spectroscopy (EDX) (MIRA 3, TESCAN at an operating voltage of 10 kV), was used to study the morphology and elemental distribution of the catalysts and electrodes. X-ray diffraction (XRD) patterns were obtained on a Rigaku Smartlab II diffractometer with a nominal 3-kW X-ray source to analyse the crystalline structure of the catalysts. An X-ray photoelectron spectroscope (XPS) (SSX-100, Surface Science Laboratories, Inc.), equipped with a monochromatic Al Kα X-ray source, was used to characterise the catalyst surface. The CGs were assembled onto carbon paper for the XRD testing, and the CG powders for XPS analysis.

2.4 Electrode Assembly

The catalyst powder (20 mg) was mixed with 1 mL ethanol in a 2-mL sample tube and sonicated for 10 min. Nafion® solution (40 µL; 5 wt.%, Sigma-Aldrich) was added to the tube and sonicated for 1 h. The as-prepared ink was spray-painted onto carbon paper (H23C6, Freudenberg) with an effective surface area of 2 cm^2. The process was repeated until the mass increased (Δm) to 5 mg cm^{-2}. The catalysts on the gas diffusion layer (GDL) were characterised using SEM/EDS.

2.5 Electrochemical Evaluation Methods

The electrochemical measurements were performed using an Autolab potentiostat/galvanostat (Metrohm Autolab PGSTAT302N). Ag/AgCl and Pt wire were used as the reference and counter electrodes, respectively. The reference electrode was converted to RHE using the following equation:

$$E_{RHE} = E_{Ag/AgCl} + 0.197\ V + 0.0591\ V \times pH \quad (1)$$

We studied the electrochemical performance of the catalysts for eCO_2RR using self-designed GDE-cells, and the full details of our 3D printed device is shown in Figure S1 in Supplementary

Information. A carbon paper GDL served as the current collector and physical substrate for the catalyst; Ag/AgCl and Pt wire were used as the reference and counter electrodes, respectively. CO_2 gas was supplied using a gas inlet into the gas chamber and then diffused across the GDL to reach the catalyst layer. The CO_2 gas flow rate was maintained at 15 mL min^{-1} using a flow meter (Cole-Parmer TMR1-010462). The influence of pH on the electrolyte was evaluated at high pH (1 M and 5 M KOH as the catholyte and anolyte, respectively) and moderate pH (1 M and 2 M $KHCO_3$ as the catholyte and anolyte, respectively). The electrolytes were pre-electrolysed before the electrochemical test using chrono-potentiometry at a constant current density of 3.5 mA cm^{-2} using Pt-mesh electrodes for purification. The pre-purge of CO_2 is not required in the electrolyte of the GDE cell. A cation exchange membrane (CEM, Fumapem F-950) was placed between the catholyte and the anode, allowing the cations to transfer through the membrane. The gas products were collected from the gas outlet, and the catholyte was collected for liquid product analysis after the reaction.

To analyse eCO_2RR behaviour using different catalysts, we performed the chronoamperometry (CA) tests at −0.4 V, −0.6 V, −0.8 V, −1.0 V and −1.2 V vs. RHE for 0.5 h, and measured the current density (*j*) vs. the proceeding time (h). The FE of the electrochemical reaction can be calculated using the input charge and processing time of the electrochemical process in CA, along with the gaseous/liquid product measurement and molar mass calculation. The FEs of the gaseous and liquid products were analysed after 4 h and 8 h of reaction.

To investigate the catalysts' hydrogen evolution reaction (HER) reactivity for the purpose of comprehensively understand the FE results, we performed the linear scanning voltammograms (LSV) at the applied potential range from −0.1 V to −1.4 V vs. RHE at a scan rate of 50 mV s^{-1} in 1 M KOH, with N_2 and CO_2 purged conditions, accordingly. The electric double layer capacitance (C_{dl}) of catalysts were estimated by CV scans in the range of −0.1 V to 0.3 V vs.

RHE in CO_2 saturated 1 M KOH, at the scan rates from 20 mV s^{-1}, 40 mV s^{-1}, 60 mV s^{-1}, 80 mV s^{-1} and 100 mV s^{-1} where no Faradaic reaction happens. The double layer capacitances were calculated using the following equation[32, 37]:

$$C_{dl} = J(\frac{dV}{dt}) \quad (2)$$

where J is the current density of 0.1 V vs. RHE, and $\frac{dV}{dt}$ is the scan rate of CVs.

To evaluate the stability of each catalyst, we performed CA tests in the GDE cell at an applied potential of −1.0 V vs. RHE in 1 M KOH with a constant CO_2 gas supply (15 mL min^{-1}). The long-term experiment was conducted for 8 h, and 100 mL catholyte was cycled throughout the reaction.

2.6 Products Analysis

The gaseous products of eCO_2RR were collected from the outlet of the reaction cell and analysed using gas chromatography (GC, Shimadzu Tracera GC-2010) coupled with a barrier discharge ionisation detector (BID). The CO_2 flow rate was maintained at 15 mL min^{-1} using a flow meter.

The liquid product (formate) was collected from the catholyte and quantified using an ion chromatography (Eco IC, Metrohm) equipped with a 'Metrohm 6.1005.200' column formic acid identification. The FE value for each product was calculated according to Faraday's law [8], and the detailed calculations are provided in the SI.

2.7 COMSOL Simulation

A multi-physics model based on COMSOL was implemented to investigate the mass transfer and electrochemical reduction of CO_2 at a given flow rate, pressure, temperature, and potential. The model consisted of an electrolyte chamber (EC), catalyst layer (CL), gas diffusion layer

(GDL), and gas chamber (GC) (Figure S2). The fluids through the chambers were assumed to have a laminar flow, and the velocity profile in the porous electrode was described using the Navier-Stokes equation. The calculated gas velocity was correlated with the convective mass transport in the convection-diffusion-reaction equation. The Butler-Volmer equation was used to correlate the relationship between current density and applied electrode potential, and Faraday's law was applied to convert the current density to the generation/consumption rates of chemical species in the system, which were used as the source/sink terms in the convection-diffusion-reaction equation. The concentrations of various species, such as $CO_{2(g)}$, $CO_{2(aq)}$, $CO_{(g)}$, and formate, current and potential distributions, and velocity profiles were correlated, and the hydrogen evolution reaction (HER) was considered as a side reaction. The detailed model development is shown in Figure S2 and Table S1.

2.8 Model Assumptions and Features

The multi-physics model was developed based on the following assumptions:

- Reactant gas flowing through the cathode channels is treated as laminar flow.
- Sufficient CO_2 was supplied evenly at a constant flow rate at the cathode inlet, and the ideal gas law was applied to the gas species.
- Temperature variation due to chemical reactions is neglected.
- Mass transport occurs through diffusive and convective mechanisms. The Soret effect for mass transport was not considered because of the isothermal assumption.
- The pH of the bulk solution at the anode remained constant, and no acid-base equilibria occurred at the catalyst layer-electrolyte boundary.
- Electrolyte conductivity is independent of the KOH concentration in the studied range.

The model considers the following processes: 1) the conservation of mass, species, charge, and momentum; 2) species transport through the porous electrode under diffusion and convection mechanisms; and 3) species generation and consumption inside the catalyst layer using electrical energy as the driving force. Additionally, the physical properties of the catalyst layer, such as thickness, pore size, and porosity, were also simulated for the catalyst morphology. The governing equations are given by Equations 3–10 and Equations S3–S11.

2.9 Governing Equations

The equations describing the conservation of momentum, mass, and species are discussed in the following section. Under the steady-state condition, the continuity equation is applied to describe the mass balance of the reactants flowing through the channel and porous electrode, leading to

$$\nabla \cdot \left(\rho_g u_g\right) = 0 \qquad (3)$$

where ρ_g and u_g are the density and velocity, respectively, of the gas mixture.

For compressive Newtonian fluids, the Navier-Stokes equation is applied to simulate the variation in velocity and pressure within the channel, resulting in

$$\rho_g\left(u_g \cdot \nabla\right)u_g = \nabla \cdot \left[-PI + u_g\left(\nabla u_g + \left(u_g\right)^T\right) - \frac{2}{3}\mu_g\left(\nabla \cdot u_g\right)I\right] + \rho_g g \qquad (4)$$

where P is the pressure, I is the identity matrix, μ_g is the dynamic viscosity of the gas mixture, and g is the gravitational acceleration. The above equation takes into account the effect of gravity on momentum balance.

The average diffusion model used in COMSOL was selected for species conservation in porous media and gas chambers, and the conservation of species is described by the following diffusion-convection-reaction equation:

$$\nabla \cdot N_i + \left(u_g \cdot \nabla\right) c_i = R_i \tag{5}$$

where N_i is the flux, c_i is the concentration, and R_i is the source/sink term of species i.

The above equation can be re-written as:

$$\nabla \cdot \left(-\rho_g D_{i,m} \nabla \omega_i - \rho_g \omega_i D_{i,m} \frac{\nabla M_g}{M_g}\right) + \nabla \cdot \left(\rho_g u_g \omega_i\right) = R_{i,m} \tag{6}$$

where ω_i is the mass fraction, M_g is the mean molar concentration of the gas mixture ($M_g = (\sum_j \frac{\omega_i}{M_i})^{-1}$), M_i is the molar concentration of species i, $D_{i,m}$ is the diffusivity of the gas mixture, which comes from the Maxwell-Stefan equation, and is calculated using $D_{i,m} = \frac{1-\omega_i}{\sum_{k \neq i} \frac{x_k}{D_{ik}}}$, x_k is the molar fraction of gas, and D_{ik} is the binary diffusivities of the species pairs.

The electrode reaction rate is controlled by charge transfer and is independent of mass transfer when the reactant supply is sufficient. The Tafel equation was chosen as the kinetic expression for the electrode, and the current density was obtained as follows:

$$i_{Ea} = -i_{o,Ea}^{ref} \left(\frac{C_{CO_2(aq)}}{C_{CO_2(aq),Ea}^{ref}}\right) \exp\left(-\frac{\beta_{Ea} F}{R_{ideal} T}\left(V_0 - V_1 - V_{eq,Ea}^{ref}\right)\right) \tag{7}$$

$$i_{Eb} = -i_{o,Eb}^{ref} \left(\frac{C_{CO_2(aq)}}{C_{CO_2(aq),Eb}^{ref}}\right) \exp\left(-\frac{\beta_{Eb} F}{R_{ideal} T}\left(V_0 - V_1 - V_{eq,Eb}^{ref}\right)\right) \tag{8}$$

$$i_{Ec} = -i_{o,Ec}^{ref} \exp\left(-\frac{\beta_{Ec}F}{R_{ideal}T}\left(V_0 - V_1 - V_{eq,Ec}^{ref}\right)\right) \quad (9)$$

where $i_{o,Ej}^{ref}(j = a, b, c)$ are the reference exchange current densities for generating HCOO, CO, and H_2, respectively, $C_{CO_2(aq),Ea}^{ref}$ and $C_{CO_2(aq),Eb}^{ref}$ are the reference concentrations for producing HCOO and CO, respectively, R_{ideal} is the ideal gas coolant; $\beta_{Ei}(i = a, b, c)$ are symmetry factors, F is the Faraday constant, and $V_{eq,Ei}^{ref}$ $(i = a, b, c)$ are equilibrium potentials.

According to Faraday's law, the electrochemical reaction rates of CO_2, HCOO, CO, and H_2 can be obtained as follows:

$$R_{E,CO_2(aq)} = \frac{M_{CO_2}a_{sl}(i_{Ea} + i_{Eb})}{2F}\ ;\ R_{E,HCOO} = -\frac{M_{HCOO}a_{sl}i_{Ea}}{2F};$$
$$R_{E,CO} = -\frac{M_{CO}a_{sl}i_{Eb}}{2F};\ R_{E,H_2} = \frac{M_{H_2}a_{sl}i_{Ec}}{2F} \quad (10)$$

where M_{CO_2}, M_{HCOO}, M_{CO}, and M_{H_2} are the molecular weights of each species, a_{sl} is the specific area of the solid-liquid interface, and an idealised structure of the catalyst layer was designed to calculate the specific area a_{sl}. The details are presented in Figure S3. The other equations can be found elsewhere [38].

3. RESULTS AND DISCUSSION

3.1 Preparation and Characterisation of the Catalysts

The SEM morphology and EDS mapping spectra of the catalysts are shown in **Figure 2**. With an increase in temperature from 70 °C to 90 °C, the opening degree of the petals increased gradually; it started with nanobuds at 70 °C and developed into nanoflowers at 90 °C. The longitudinal length of CGs range between 1.3 μm and 1.7 μm, and the diameter of each petal is 40 nm. For comparison, the Cu_2O nanoparticle was characterised (Figure S4a), and they demonstrated a cubic shape with an average particle size of 100 nm. The EDS mappings of CGs1–5 were studied for elemental analysis (Figures 2 f–o) and indicated an even distribution of Cu and O throughout the nanoparticles.

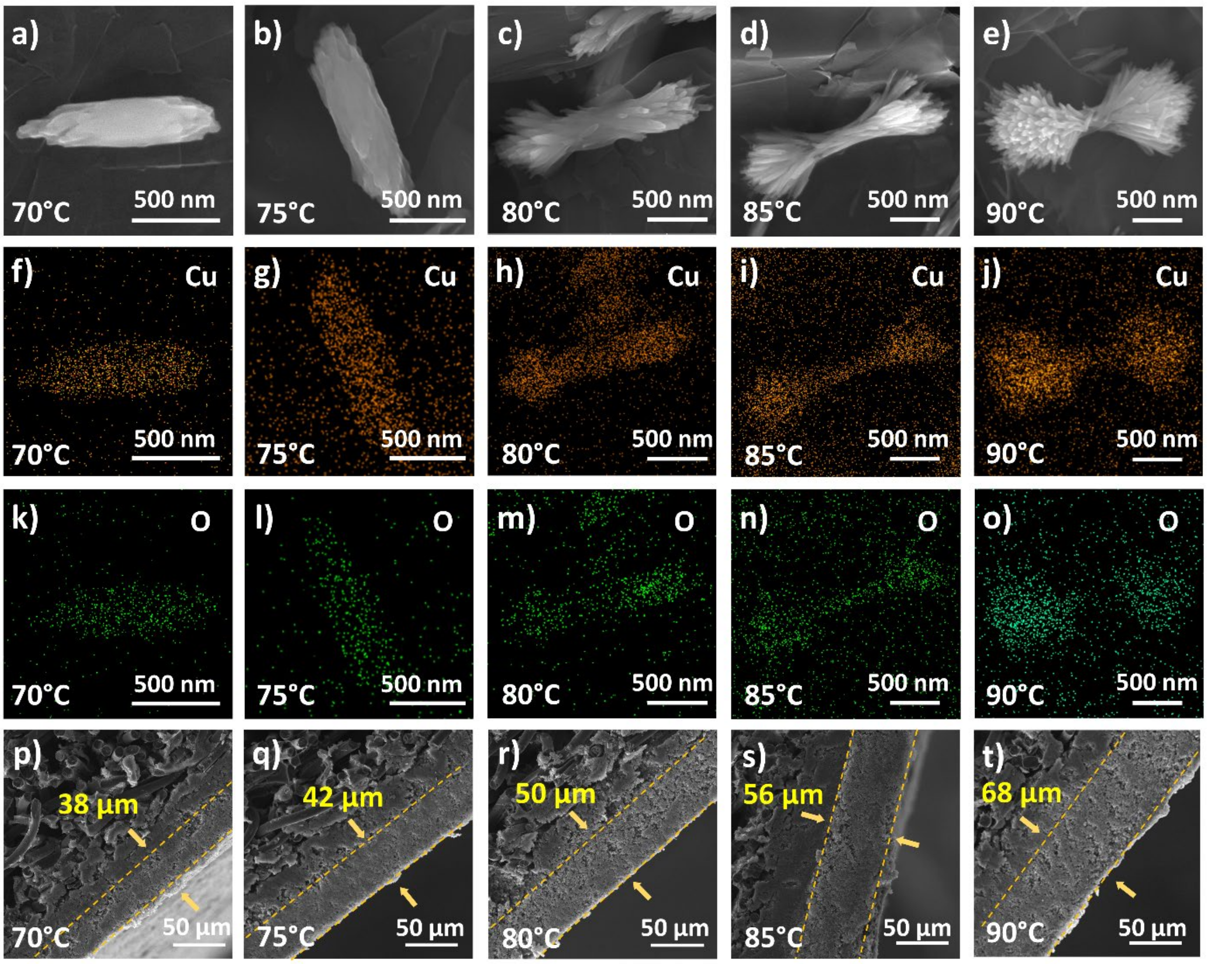

Figure 2 SEM scanning of a–e) Cu_2O nanoparticles on CG1–5 catalysts; EDS mapping of the composition of samples CG1–5; f–j) Cu and k–o) O elemental distribution; p–t) Thickness of catalyst layer via cross-section view of CGs1–5 assembled electrode.

SEM was used to study the cross-sectional morphology of all the gas diffusion electrodes to calculate the thickness of each CG catalyst layer (Figures 2 p–t). The electrodes were assembled with the same catalyst weight loading and coating area. The thickness of the CG catalysts increased with increasing degree of flower opening, indicating a reduction in the density and increase in the porosity of the catalyst layer with increasing thickness. The catalyst layer of the CGs exhibited a 'sponge' layer rather than a 'compressed layer', and the average thicknesses of CGs1–5 were 38 μm, 42 μm, 50 μm, 56 μm, and 68 μm, respectively. The catalyst layer thickness for the cubic Cu_2O catalyst was 18 μm (Figure S4b).

The crystal structure and atomic structure of the CG catalysts were analysed using XRD and XPS (**Figure 3**). The XRD pattern of all CG catalysts (Figure 3a) shows identical characteristic diffraction peaks of Cu_2O at 2θ = 30°, 36°, 42°, 61°, 74°, and 78°, corresponding to (110),

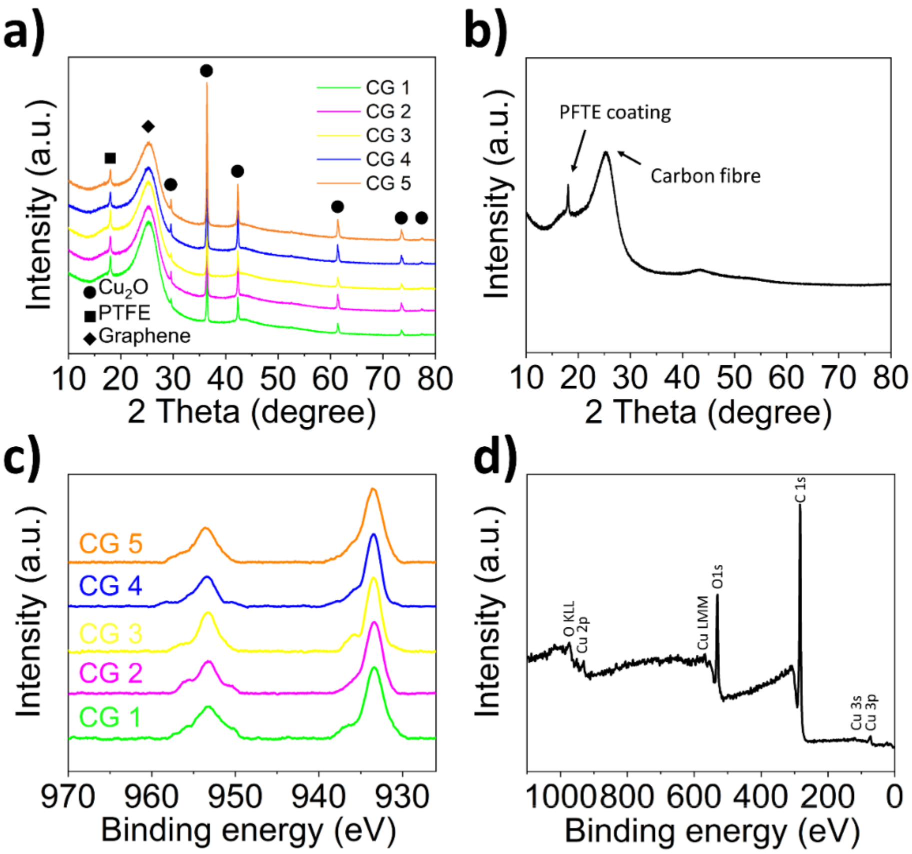

Figure 3 XRD patterns of a) CG electrodes, b) PTFE coated carbon paper as gas diffusion layer, c) XPS spectra of Cu 2p regions of CG catalysts and d) XPS survey spectrum of CG catalysts

(111), (200), (220), (311), and (222) planes, respectively; the peak at 2θ = 18° indicates the PTFE coating on carbon paper (Figure 3b), while the broad peak at 2θ = 25° corresponds to graphene. In our experiments, the crystallinity of the catalysts did not influence the CG catalysts performance themselves. To further prove this observation, the average crystallite size was calculated using XRD and shown in Table S2, where all CG catalysts present similar average crystallite size of ca. 31 nm. The XPS Cu 2p spectra of CGs 1–5 are shown in Figure 3c, where the Cu-related peaks are symmetric. The absence of satellite structure at 943 eV rules out Cu^{2+} in the CG catalysts [39]. The two apparent peaks at 933 eV and 953 eV are attributed to the Cu2p3/2 and Cu2p1/2 peaks, respectively, of the Cu^{+} in Cu_2O. The XPS results were consistent for all the catalysts. The XPS survey spectra of CGs 1–5 present a similar pattern (Figure 3d), confirming the presence of copper, oxygen, and carbon species. The XRD and XPS results confirmed the similar crystal and atomic structure of these five CG catalysts, indicating that the effect on eCO_2RR performance of CG1–CG5 depends purely on the catalyst morphology-induced catalyst layer property variations.

3.2 COMSOL Simulation of Catalyst Layer for eCO_2RR

The effect of different catalyst layers was simulated to study the properties of CG catalysts for eCO_2RR and to analyse the mass transfer and conversion of CO_2 gas within the cells. The CO_2 molar concentrations in the gas chamber and the gas velocity inside the catalyst layers were investigated mathematically using the model developed in COMSOL Multiphysics®.

We calculated the specific interfacial area of each CG catalyst layer, which corresponds to the porosity of each CG catalyst. The pore sizes of the CG catalysts (29, 32, 35, 37, and 40 µm corresponding to CGs1–5, respectively) were calculated using Equations S7 and S8 (Figure 4a). The specific interfacial area exhibited a strong linear relationship with the pore radius. The slope of the linear fitting of the solid-liquid (catalyst layer-electrolyte) interface indicates a minor influence of the pore size of the catalyst layer on the solid-liquid interface. The gas-liquid (CO_2-electrolyte) interface improves with increasing pore size, resulting in enhanced

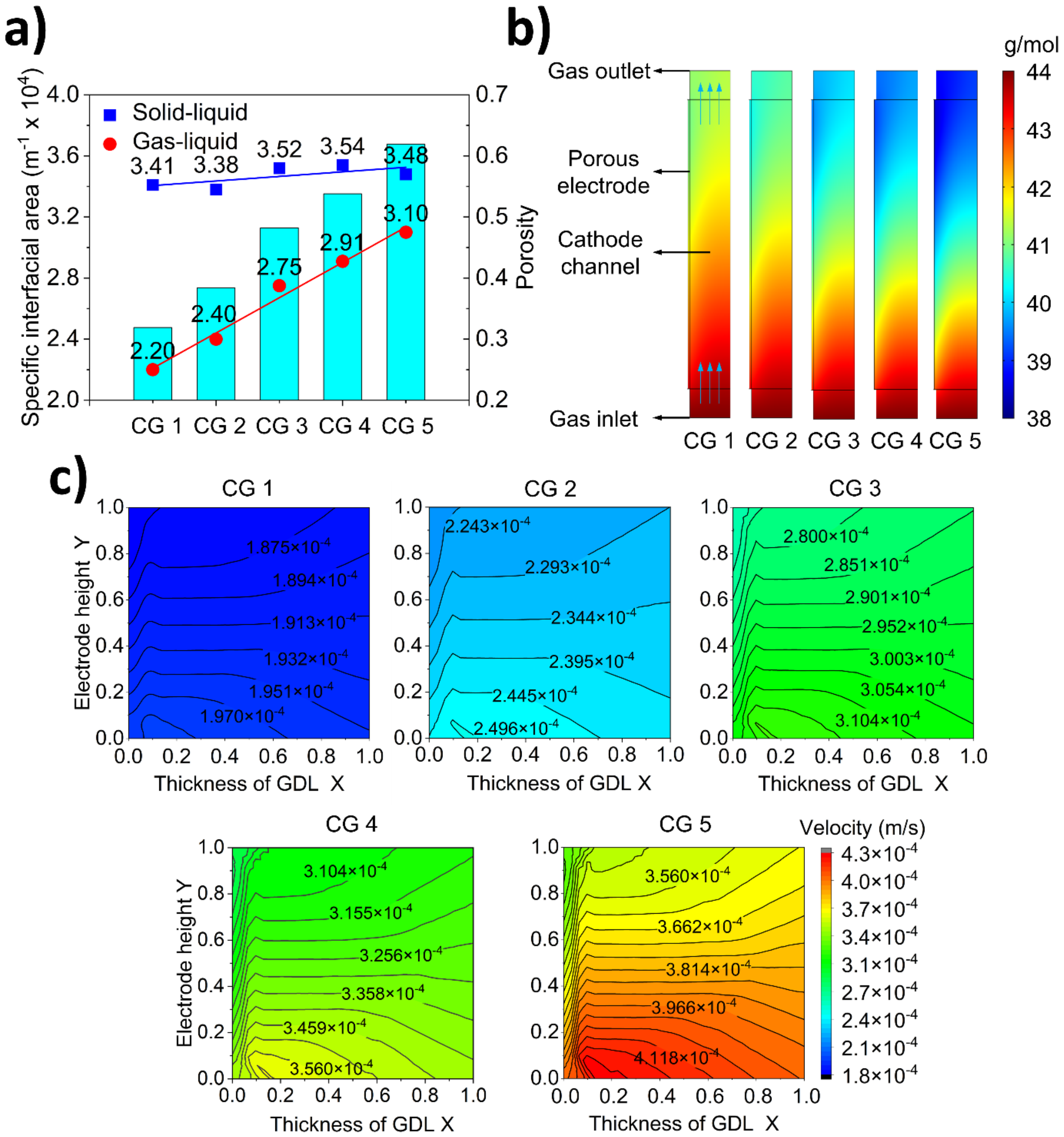

Figure 4 a) Specific interfacial area of CG catalysts layer (line-plot correspond to specific interfacial area, and the column plot correspond to porosity). b) Mean molar mass in CG, GDL, CL at −1.0 V vs. RHE, where the upper and bottom boxes represent the outlet and inlet of the gas chamber, the cylinder in the middle is the gas chamber. The thin layer attached to GDL on the left side is CL which has different parameters. c) Average CO_2 gas flow velocity in GDL at −1.0 V vs. RHE, where X = 0 for the 'CL-GDL' interface, X = 1 for the 'GDL-gas chamber' interface. Y = 0 for cathode inlet, Y = 1 for cathode outlet.

mass transfer rate of CO_2 from the gaseous to aqueous phase owing to the increased contact area between CO_2 and the electrolyte.

Figure 4b shows the CO_2 mass concentration within the GDE cell, and the CO_2 concentration declines across the top half of the chambers from CG1 to CG5. The CG5 catalyst exhibited the lowest CO_2 concentration near the outlet of the gas chamber, indicating the highest CO_2 consumption in CG5. Therefore, CG5 demonstrates the highest mass transfer and reaction efficiency and FE toward CO. The CO_2 gas velocity in the GDE cell at an applied potential of −1.0 V vs. RHE, corresponding to eCO_2RR, is shown in Figures 4c. X = 0 indicates the interface between the carbon paper/GDL and catalyst layer, and X = 1 corresponds to the interface between the catalyst layer and gas chamber. Y = 0 and Y = 1 represent the boundaries of the GDL near the gas inlet and outlet, respectively. CG5 exhibited the highest velocity within the GDL on account of its highest porosity. The velocity peaks near X = 0.1 correspond to the partial blockage of the CO_2 flow due to CL, resulting in velocity loss. The higher velocity near the gas inlet compared to the gas outlet can be attributed to the loss of gas fluid momentum owing to the CO_2 captured inside the porous electrode, including GDL and CL. The simulation results indicated a linear correlation between the nanoflower opening degree and the porosity and surface/volume ratio. The improved gas velocity indicated enhanced mass transport via a convective mechanism, which accelerated the dissolution of gaseous CO_2 into the electrolyte and increased the concentration of aqueous CO_2 resulting in fast eCO_2RR kinetics. The increased specific area changes the internal structure of the catalyst layer by creating more pores that trap the reactant gas (CO_2) within the catalyst layer, forming a robust gas-liquid-solid interface for eCO_2RR. Additionally, the porous catalyst also mitigates the GDL flooding[40]. The results indicate higher CO_2 absorption and higher CO_2 velocity within the catalyst layer due to the increased specific area and porosity, which improve the CO_2 reaction and mass transport activity.

3.3 Electrochemical CO_2 Reduction Reaction of CG Catalysts in GDE Cell

The eCO_2RR properties of all the CG catalysts were evaluated using a GDE cell reaction system, and the FE results of the CG catalysts and Cu_2O cubic nanoparticles in 1 M KOH are shown in **Figure 5**. The total current density and CO partial current density are shown in **Figure 6**, and the detailed data with error analysis are available in Tables S3–S10. The lower FEs for CO in the bud-shaped CG1 catalyst correspond to 56.53%, 59.23%, 63.91%, 68.97% and 67.18% at −0.4 V, −0.6 V, −0.8 V, −1.0 V, and −1.2 V vs. RHE, respectively. CG1 also exhibits the lowest current density due to the reduced surface area/volume ratio, which reduces the number of active sites on the surface. The FE and current density of carbonaceous products increase from CG1 to CG5 because of the increase in active sites on the catalyst surface and enhanced porosity of the catalyst layer, which promote the reaction activity and CO_2 mass transfer. The increased porosity of CG5 resulted in increased surface area of the solid-liquid and gas-liquid interfaces and enhanced the reaction. The FEs at −0.4 V, −0.6 V, −0.8 V, −1.0 V, and −1.2 V vs. RHE are 74.43%, 79.84%, 87.26%, 93.20%, and 91.14%, respectively. The

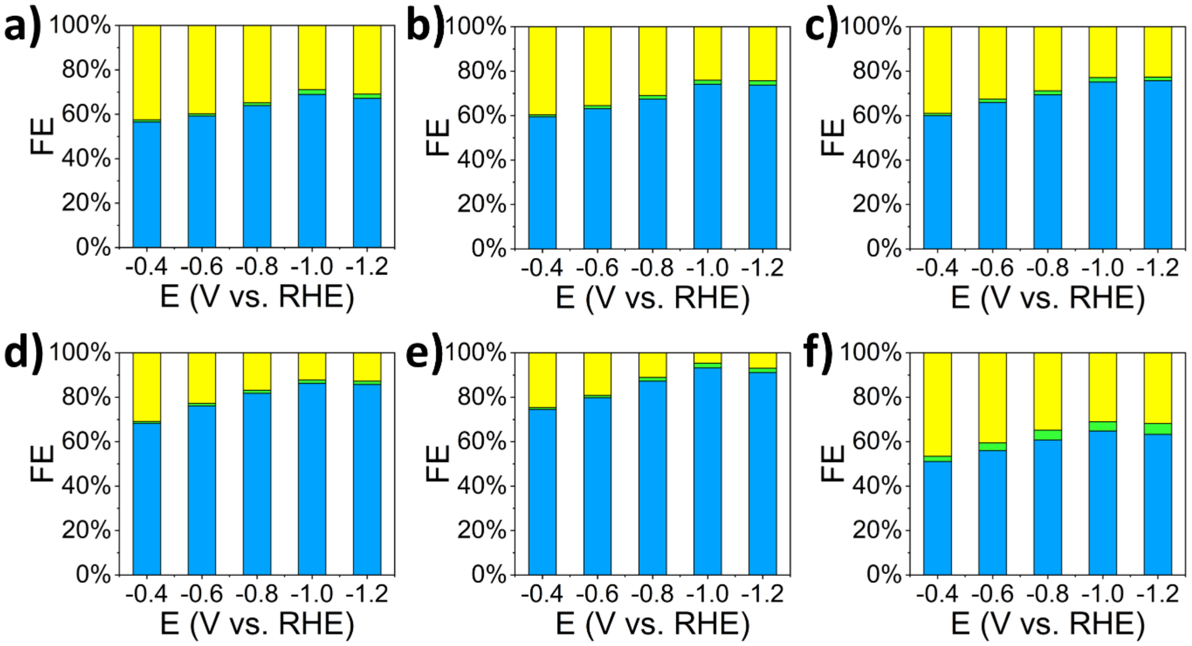

Figure 5 Faradaic efficiency profiles of a–e) CGs1–5 and f) Cu_2O in 1 M KOH electrolyte for eCO_2RR with products including CO (blue), formate (green), and H_2 (yellow)

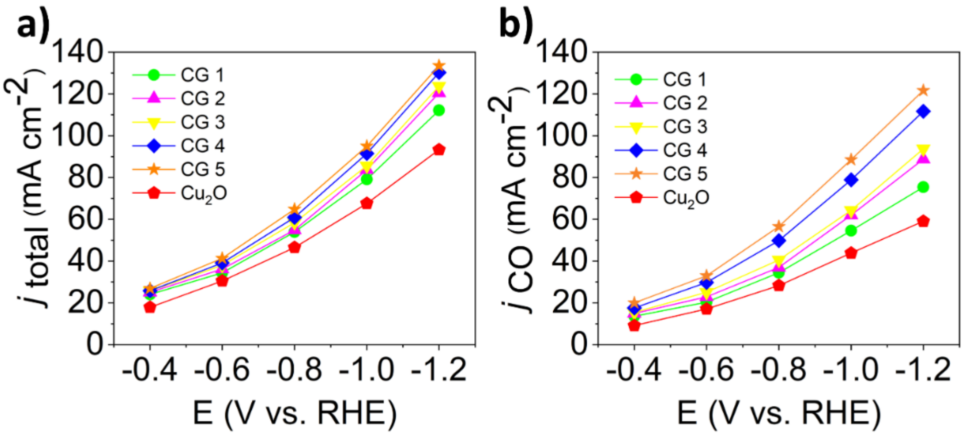

Figure 6 a) Total current density and b) current density of CO for CGs1–5 and Cu_2O in 1 M KOH electrolyte.

Cu_2O exhibited lower activity and selectivity toward eCO_2RR compared to the CG catalysts. The graphene in the CG catalysts separate the Cu_2O and provides a better gas-liquid-solid interface, thereby promoting charge transfer and CO_2 mass transfer within the catalyst layer. Contrastingly, pure Cu_2O (Figure 5f) does not form a porous structure within the catalyst layers, which reduces the CO_2 mass transfer and promotes the HER, resulting in poor eCO_2RR [36]. The FEs at −0.4 V, −0.6 V, −0.8 V, −1.0 V, and −1.2 V vs. RHE are 51.07%, 55.98%, 60.80%, 64.85% and 63.31%, respectively. Additionally, the crystal structures also affect the composition of gaseous and liquid products.

To further investigate the performance of CG catalysts in eCO_2RR, we performed LSV for all CG catalysts and Cu_2O. The results are shown in Figure S5a. In N_2-fed condition, all catalysts present a trend of lower current densities at less negative potentials, and gradually increased at higher potentials contributed by HER. While in CO_2-fed condition, the current density increases sharply at higher potentials where CO_2RR happens and supresses the HER. The CG5 presents the highest reaction activity, which agrees well with FE measurement. The statements were confirmed by measuring the double-layer capacitances (C_{dl}) under different scanning rates. As shown in Figure S5b, the C_{dl} of CGs increases from CG1 to CG5, by enhancing their internal porosity, and the C_{dl} of CG5 presents over 6 times than that of Cu_2O. It is believed that the presence of graphene allows the nanoflower evenly distributed on the surface and avoid the agglomeration which enhanced its surface active sites. Figure S5c shows the Tafel parameters of different CGs and Cu_2O for eCO_2RR. All Tafel slopes are lower than 118 mV dec^{-1}, which suggests the same mechanism for CO_2 reduction reaction[32]. With increased porosity and changed morphology of the catalysts, the Tafel plots were decreased from 82.1 mV dec^{-1} to 70.7 mV dec^{-1}, indicating faster kinetics and higher activity of eCO_2RR.

Above results indicate the synergistic effect between the Cu_2O nanoflower and graphene sheets on the catalyst layer enhances the conversion of CO_2 to carbonaceous products. Initially, the CG catalyst forms a porous layered structure that enhances the CO_2 retention and CO_2 mass transfer. Additionally, the porous catalyst layer enhances the internal hydrophobicity and prevents electrode flooding by electrolyte. The Cu_2O-graphene interaction changes the electronic structure [41], and the Cu_2O particles prevent the HER in graphene, resulting in a 2D surface sufficient for Cu_2O to distribute and enhance the surface area of the proton-enriched electrode. The combined effects of these factors yield improved eCO_2RR results.

The eCO_2RR was performed at moderate pH to study the effect of electrolyte alkalinity in aqueous electrochemical CO_2 reduction using CG catalysts (Figure S6). Within the potential range from −0.4 V to −1.2 V vs. RHE, the FE and current density of carbonaceous products increase from CG1 to CG5, aligning well with the 1 M KOH electrolyte results. The CG5 with nanoflower-shaped structure (Figure S6e) exhibits the FE of 53.11%, 63.90%, 70.12%, 72.72% and 71.82% at −0.4 V, −0.6 V, −0.8 V, −1.0 V, and −1.2 V vs. RHE, respectively. The FEs of Cu_2O (Figure S6f) at potentials of −0.4 V, −0.6 V, −0.8 V, −1.0 V, and −1.2 V vs. RHE are 21.56%, 34.31%, 47.87%, 52.90% and 54.71%, respectively.

Owing to the increase in surface area and porosity, the FE and current density of the carbonaceous products increases from CG2 through CG3 to CG4 (Figures S6 b–d). The current density and FE of carbonaceous products for 1 M $KHCO_3$ were lower than 1 M KOH. The strong base electrode suppresses HER and promotes eCO_2RR [22]. The results in 1 M $KHCO_3$ confirm that the eCO_2RR can be enhanced using catalysts with higher active sites and a porous structure. The detailed data and relevant random errors are listed in Tables S11–S18. The simulation can be applied to any reaction regardless of the electrolyte.

3.4 Stability Evaluation of CG Catalysts in GDE Cell

The stability of the eCO_2RR reaction system is essential for commercial implementation because the GDLs may lose their hydrophobicity and permeate by electrolyte after a long-term

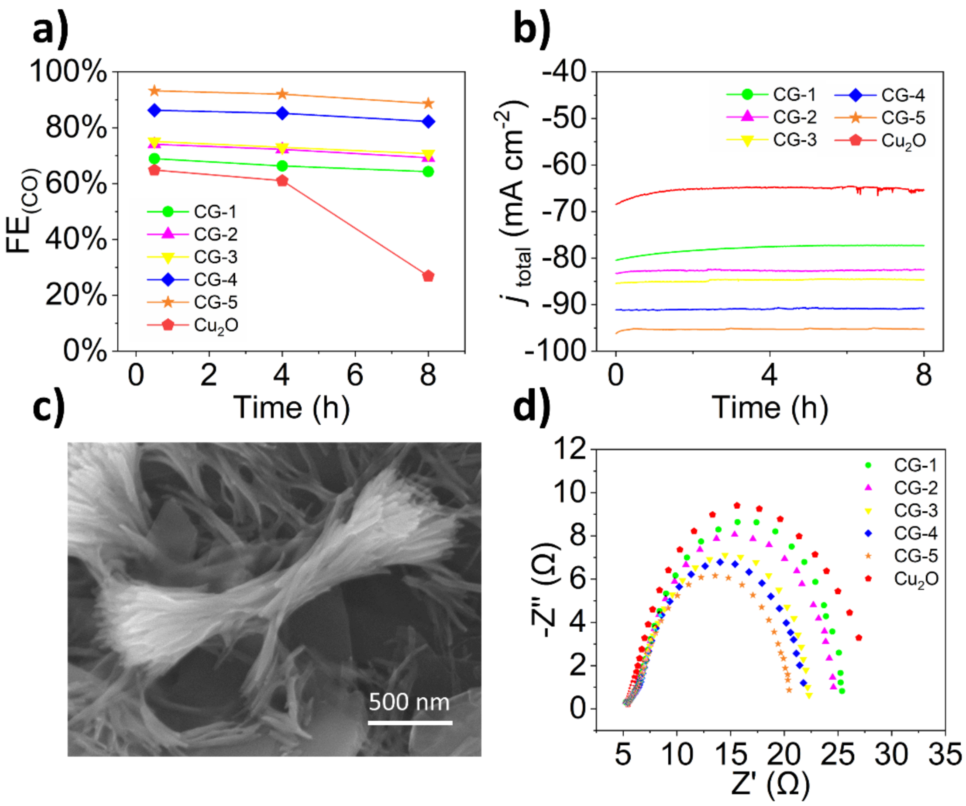

Figure 7 a) FE_{CO} results of stability test after 0.5 h, 4 h, and 8 h reaction of the CG catalysts at −1.0 V vs. RHE. b) Stability tests of CGs1–5 and Cu_2O at −1.0 V vs. RHE for 8 h in 1 M KOH, GDE system. c) SEM image of CG5 after 8 h reaction. d) Electrochemical impedance spectroscopy of CG catalysts and Cu_2O in 1 M KOH.

reaction [42]. The CG catalysts retain good FE of CO (**Figure 7)** after the 4-h and 8-h tests compared to the half-hour reaction (Figure 7a, detailed data and relevant random error are listed in Tables S19 and S20). The current remains stable after 8 h, and the FE values of CO for CGs1–5 after 8 h of reaction were 64.30%, 69.26%, 70.69%, 82.23%, and 88.69%, respectively. The hydrophobic porous CG catalyst layer prevents electrolyte penetration during the reaction. The increase in thickness of the hydrophobic layer from CGs1–5 reduces the electrolyte permeation through the GDL. The enhanced porosity of the catalyst layer increases the gas-liquid-solid (CO_2-electrolyte-catalyst) interface, which enhances the active sites for eCO_2RR. Conversely, the FEs decreased significantly after 8 h of reaction using Cu_2O, and the corresponding FE of CO is 26.91%. Additionally, the CA plot becomes unstable due to electrode permeation. To further explore the reason for the stability of the CG catalysts, we scanned the CG5 electrodes using SEM after the reaction (Figure 7c). The CG retains the nanoflower shape, even though the outer layers fall on the graphene sheets. Therefore, the catalyst retains a high surface area for the reaction. Cu_2O nanoparticles exhibited a reduced FE due to the damage of the catalyst surface (Figure S7) owing to the electrochemical corrosion, which reduces the number of active sites on its surface and reduces the eCO_2RR performance. Impedance spectroscopy was performed on CG catalysts and Cu_2O cubic catalyst at 0.1 V vs. RHE to study the charge transfer of the CG catalysts (Figure 7d). The Nyquist plots indicate an increasing trend for all the CG catalysts with the blooming process. The increase in porosity of the catalysts improves the internal charge transfer, which results in enhanced eCO_2RR performance. In contrast, the Cu_2O exhibited higher internal resistance, leading to a lower current density for the eCO_2RR.

4. CONCLUSIONS

We developed an architecture-controlled catalyst for the electrochemical conversion of CO_2 to CO. The temperature-dependent CG catalysts with controllable morphologies enhance the

eCO_2RR activity and efficiency by enhancing the gas-liquid and liquid-solid specific areas and the porosity of the catalyst layer. Increasing the concentration of the incoming CO_2 near the catalyst layer surface increased the CO_2 concentration within the catalyst layer and enhanced the CO_2 velocity in the gas chamber, thereby improving the eCO_2RR. The enhanced hydrophobicity of the catalyst layer provided considerable stability to the eCO_2RR system. FE higher than 90% for CO and formate was obtained for CG5 catalyst at −1.0 V vs. RHE in a 1 M KOH electrolyte. The highly porous catalyst layer is hydrophobic and prevents the GDL from being flooded, thereby enhancing the stability with a low FE drop after 8 h of reaction. The enhanced conductivity and active sites of CG5 promote the reaction activity at a current density of 133.5 mA cm^{-2} and applied potential of −1.2 V vs. RHE.

Although the catalyst did not form the desired nano-bud or nanoflower structure at temperatures below 70 °C and above 90 °C from the experimental aspect, this study has established a theoretical analysis of the relationship between the CL intensity/mass transfer and the induced eCO_2RR performance.

ACKNOWLEDGMENTS

This work was supported by the UK Engineering Physics and Science Research Council (Grant No. EP/S032886/1), and the Royal Society International Exchanges Award (Grant No. IEC\NSFC\201008)

SUPPORTING INFORMATION

Supporting Information is available from xxx.

DECLARATION OF INTERESTS

There are no conflicts to declare.

REFERENCES

[1] T. Wilberforce, A. Olabi, E.T. Sayed, K. Elsaid, M.A. Abdelkareem, Progress in carbon capture technologies, Science of The Total Environment, (2020) 143203.
[2] A.I. Osman, M. Hefny, M. Abdel Maksoud, A.M. Elgarahy, D.W. Rooney, Recent advances in carbon capture storage and utilisation technologies: a review, Environmental Chemistry Letters, 19 (2021) 797-849.
[3] P. Renforth, The negative emission potential of alkaline materials, Nature communications, 10 (2019) 1-8.
[4] L. Xing, R.C. Darton, A. Yang, Enhanced weathering to capture atmospheric carbon dioxide: Modeling of a trickle-bed reactor, AIChE Journal, 67 (2021) e17202.
[5] J. Fu, K. Jiang, X. Qiu, J. Yu, M. Liu, Product selectivity of photocatalytic CO_2 reduction reactions, Materials Today, 32 (2020) 222-243.
[6] G. Zhao, X. Huang, X. Wang, X. Wang, Progress in catalyst exploration for heterogeneous CO_2 reduction and utilization: a critical review, Journal of Materials Chemistry A, 5 (2017) 21625-21649.
[7] J. Qiao, Y. Liu, F. Hong, J. Zhang, A review of catalysts for the electroreduction of carbon dioxide to produce low-carbon fuels, Chem Soc Rev, 43 (2014) 631-675.
[8] D.D. Zhu, J.L. Liu, S.Z. Qiao, Recent advances in inorganic heterogeneous electrocatalysts for reduction of carbon dioxide, Advanced materials, 28 (2016) 3423-3452.
[9] Y. Zheng, A. Vasileff, X. Zhou, Y. Jiao, M. Jaroniec, S.-Z. Qiao, Understanding the roadmap for electrochemical reduction of CO_2 to multi-carbon oxygenates and hydrocarbons on copper-based catalysts, Journal of the American Chemical Society, 141 (2019) 7646-7659.
[10] S. Liang, N. Altaf, L. Huang, Y. Gao, Q. Wang, Electrolytic cell design for electrochemical CO_2 reduction, Journal of CO_2 Utilization, 35 (2020) 90-105.
[11] D.C. Grills, Y. Matsubara, Y. Kuwahara, S.R. Golisz, D.A. Kurtz, B.A. Mello, Electrocatalytic CO_2 Reduction with a Homogeneous Catalyst in Ionic Liquid: High Catalytic Activity at Low Overpotential, J Phys Chem Lett, 5 (2014) 2033-2038.
[12] H.A. Hansen, J.B. Varley, A.A. Peterson, J.K. Norskov, Understanding Trends in the Electrocatalytic Activity of Metals and Enzymes for CO_2 Reduction to CO, J Phys Chem Lett, 4 (2013) 388-392.
[13] S. Nitopi, E. Bertheussen, S.B. Scott, X. Liu, A.K. Engstfeld, S. Horch, B. Seger, I.E. Stephens, K. Chan, C. Hahn, Progress and perspectives of electrochemical CO_2 reduction on copper in aqueous electrolyte, Chemical reviews, 119 (2019) 7610-7672.

[14] T. Hatsukade, K.P. Kuhl, E.R. Cave, D.N. Abram, T.F. Jaramillo, Insights into the electrocatalytic reduction of CO(2) on metallic silver surfaces, Phys Chem Chem Phys, 16 (2014) 13814-13819.

[15] W. Zhang, Y. Hu, L. Ma, G. Zhu, Y. Wang, X. Xue, R. Chen, S. Yang, Z. Jin, Progress and Perspective of Electrocatalytic CO2 Reduction for Renewable Carbonaceous Fuels and Chemicals, Adv Sci (Weinh), 5 (2018) 1700275.

[16] R. Francke, B. Schille, M. Roemelt, Homogeneously Catalyzed Electroreduction of Carbon Dioxide-Methods, Mechanisms, and Catalysts, Chem Rev, 118 (2018) 4631-4701.

[17] C.-H. Huang, C.-S. Tan, A review: CO2 utilization, Aerosol and Air Quality Research, 14 (2013) 480-499.

[18] X. Xiaoding, J. Moulijn, Mitigation of CO2 by chemical conversion: plausible chemical reactions and promising products, Energy & Fuels, 10 (1996) 305-325.

[19] C.M. Gabardo, C.P. O'Brien, J.P. Edwards, C. McCallum, Y. Xu, C.-T. Dinh, J. Li, E.H. Sargent, D. Sinton, Continuous carbon dioxide electroreduction to concentrated multi-carbon products using a membrane electrode assembly, Joule, 3 (2019) 2777-2791.

[20] J. Durst, A. Rudnev, A. Dutta, Y. Fu, J. Herranz, V. Kaliginedi, A. Kuzume, A.A. Permyakova, Y. Paratcha, P. Broekmann, Electrochemical CO2 reduction–a critical view on fundamentals, materials and applications, CHIMIA International Journal for Chemistry, 69 (2015) 769-776.

[21] T. Zheng, K. Jiang, N. Ta, Y. Hu, J. Zeng, J. Liu, H. Wang, Large-scale and highly selective CO2 electrocatalytic reduction on nickel single-atom catalyst, Joule, 3 (2019) 265-278.

[22] H. Xiang, S. Rasul, K. Scott, J. Portoles, P. Cumpson, H.Y. Eileen, Enhanced selectivity of carbonaceous products from electrochemical reduction of CO2 in aqueous media, Journal of CO2 Utilization, 30 (2019) 214-221.

[23] Y. Peng, T. Wu, L. Sun, J.M.V. Nsanzimana, A.C. Fisher, X. Wang, Selective Electrochemical Reduction of CO2 to Ethylene on Nanopores-Modified Copper Electrodes in Aqueous Solution, ACS Appl Mater Interfaces, 9 (2017) 32782-32789.

[24] Y. Fu, Y. Li, X. Zhang, Y. Liu, J. Qiao, J. Zhang, D.P. Wilkinson, Novel hierarchical SnO 2 microsphere catalyst coated on gas diffusion electrode for enhancing energy efficiency of CO 2 reduction to formate fuel, Applied Energy, 175 (2016) 536-544.

[25] N. Nilius, H. Fedderwitz, B. Gross, C. Noguera, J. Goniakowski, Incorrect DFT-GGA predictions of the stability of non-stoichiometric/polar dielectric surfaces: the case of Cu2O(111), Phys Chem Chem Phys, 18 (2016) 6729-6733.

[26] G.H. Jeong, Y.C. Tan, J.T. Song, G.-Y. Lee, H.J. Lee, J. Lim, H.Y. Jeong, S. Won, J. Oh, S.O. Kim, Synthetic multiscale design of nanostructured Ni single atom catalyst for superior CO2 electroreduction, Chemical Engineering Journal, 426 (2021) 131063.

[27] W. Zhang, Y. Hu, L. Ma, G. Zhu, Y. Wang, X. Xue, R. Chen, S. Yang, Z. Jin, Progress and perspective of electrocatalytic CO2 reduction for renewable carbonaceous fuels and chemicals, Advanced Science, 5 (2018) 1700275.

[28] J. Rosen, G.S. Hutchings, Q. Lu, S. Rivera, Y. Zhou, D.G. Vlachos, F. Jiao, Mechanistic insights into the electrochemical reduction of CO2 to CO on nanostructured Ag surfaces, Acs Catalysis, 5 (2015) 4293-4299.

[29] J. Wu, Y. Huang, W. Ye, Y. Li, CO2 reduction: from the electrochemical to photochemical approach, Advanced Science, 4 (2017) 1700194.

[30] H. Mistry, A.S. Varela, C.S. Bonifacio, I. Zegkinoglou, I. Sinev, Y.-W. Choi, K. Kisslinger, E.A. Stach, J.C. Yang, P. Strasser, Highly selective plasma-activated copper catalysts for carbon dioxide reduction to ethylene, Nature communications, 7 (2016) 1-9.

[31] P. Yang, Z.J. Zhao, X. Chang, R. Mu, S. Zha, G. Zhang, J. Gong, The functionality of surface hydroxy groups on the selectivity and activity of carbon dioxide reduction over cuprous oxide in aqueous solutions, Angewandte Chemie, 130 (2018) 7850-7854.
[32] H. Rabiee, L. Ge, X. Zhang, S. Hu, M. Li, S. Smart, Z. Zhu, Z. Yuan, Shape-tuned electrodeposition of bismuth-based nanosheets on flow-through hollow fiber gas diffusion electrode for high-efficiency CO2 reduction to formate, Applied Catalysis B: Environmental, 286 (2021) 119945.
[33] W. Zhu, S. Kattel, F. Jiao, J.G. Chen, Shape-controlled CO2 electrochemical reduction on nanosized Pd hydride cubes and octahedra, Advanced Energy Materials, 9 (2019) 1802840.
[34] C.-T. Dinh, T. Burdyny, M.G. Kibria, A. Seifitokaldani, C.M. Gabardo, F.P.G. De Arquer, A. Kiani, J.P. Edwards, P. De Luna, O.S. Bushuyev, CO2 electroreduction to ethylene via hydroxide-mediated copper catalysis at an abrupt interface, Science, 360 (2018) 783-787.
[35] F.P.G. De Arquer, C.-T. Dinh, A. Ozden, J. Wicks, C. McCallum, A.R. Kirmani, D.-H. Nam, C. Gabardo, A. Seifitokaldani, X. Wang, CO2 electrolysis to multicarbon products at activities greater than 1 A cm− 2, Science, 367 (2020) 661-666.
[36] Y. Wang, H. Lei, H. Xiang, Y. Fu, C. Xu, Y. Jiang, B.B. Xu, E.H. Yu, C. Gao, T.X. Liu, Porous Bilayer Electrode Guided Gas Diffusion for Enhanced CO2 Electrochemical Reduction, Advanced Energy and Sustainability Research, (2021) 2100083.
[37] H. Rabiee, X. Zhang, L. Ge, S. Hu, M. Li, S. Smart, Z. Zhu, Z. Yuan, Tuning the product selectivity of the Cu hollow fiber gas diffusion electrode for efficient CO2 reduction to formate by controlled surface Sn electrodeposition, ACS applied materials & interfaces, 12 (2020) 21670-21681.
[38] Z. Yang, D. Li, L. Xing, H. Xiang, J. Xuan, S. Cheng, E.H. Yu, A. Yang, Modeling and Upscaling Analysis of Gas Diffusion Electrode-Based Electrochemical Carbon Dioxide Reduction Systems, ACS Sustainable Chemistry & Engineering, 9 (2020) 351-361.
[39] J. Li, Z. Mei, L. Liu, H. Liang, A. Azarov, A. Kuznetsov, Y. Liu, A. Ji, Q. Meng, X. Du, Probing defects in nitrogen-doped Cu 2 O, Scientific reports, 4 (2014) 1-6.
[40] Z.-Z. Niu, F.-Y. Gao, X.-L. Zhang, P.-P. Yang, R. Liu, L.-P. Chi, Z.-Z. Wu, S. Qin, X. Yu, M.-R. Gao, Hierarchical Copper with Inherent Hydrophobicity Mitigates Electrode Flooding for High-Rate CO2 Electroreduction to Multicarbon Products, Journal of the American Chemical Society, (2021).
[41] M.B. Ross, P. De Luna, Y. Li, C.-T. Dinh, D. Kim, P. Yang, E.H. Sargent, Designing materials for electrochemical carbon dioxide recycling, Nature Catalysis, 2 (2019) 648-658.
[42] J. Park, H. Oh, T. Ha, Y.I. Lee, K. Min, A review of the gas diffusion layer in proton exchange membrane fuel cells: durability and degradation, Applied Energy, 155 (2015) 866-880.